Heat-dissipation decomposition and free-energy generation in a nonequilibrium dot with multiple electron states

Chloe Salhani, Kensaku Chida, Takase Shimizu, and Toshiaki Hayashi
Basic Research Laboratories, NTT Inc., Kanagawa, Japan

Katsuhiko Nishiguchi*
Institute for Multidisciplinary Sciences, Yokohama National University, Kanagawa, Japan

(Received 28 January 2025; revised 16 December 2025; accepted 25 April 2026; published 26 May 2026)

We experimentally demonstrate the decomposition of heat dissipation during free-energy generation in a nanometer-scale dot transitioning to a nonequilibrium steady state via single-electron counting statistics. An alternating-current signal driving a reservoir that injects multiple electrons into the dot makes it nonequilibrium, leading to free-energy generation, heat dissipation, and Shannon-entropy production. By analyzing the time-domain probability distributions of multielectron states of the dot, we quantitatively decompose the heat dissipation into housekeeping and excess heats, thereby revealing their direct correlation with free-energy generation. This correlation suggests that the ratio of the generated free energy to the work applied to the dot can potentially reach 0.5 under far-from-equilibrium conditions induced by a large signal, while an efficiency of 0.25 was experimentally achieved. These results establish a quantitative link between decomposed heat dissipation and free-energy generation in a multielectron stochastic system, providing a thermodynamic framework for nonequilibrium electronic devices.

DOI: 10.1103/947j-vvk2

I. INTRODUCTION

Thermodynamics provides essential insights into the energetic limits of physical systems, such as the Landauer bound on information processing [1]. Experimental tests in microscopic platforms have confirmed these principles primarily under near-equilibrium conditions [2–8]. In contrast, electronic devices typically operate far from equilibrium to achieve high speed, output, and efficiency [9–12], motivating a corresponding extension of energetic limits to this regime.

A nonequilibrium state arises when an external force breaks global detailed balance and produces entropy, leading to free-energy generation as a key thermodynamic output. Within stochastic thermodynamics, this entropy production consists of heat dissipation and a change in Shannon entropy, which encodes the information content of the system and contributes to nonequilibrium free energy [13]. To analyze transitions between nonequilibrium steady states (NESSs), it is further useful to decompose the entropy production into excess and housekeeping parts: The former reflects the energetic cost to drive the system away from a steady state, while the latter quantifies the dissipation required to sustain an NESS [14–17]. This decomposition underpins nonequilibrium inequalities and fluctuation relations [15,16,18–22]. However, how the decomposed contributions quantitatively relate to free-energy generation remains experimentally unexplored.

Electronic devices provide well-controlled experiments on nonequilibrium physics: In particular, single-electron devices composed of quantum dots have enabled precise measurements of work and heat under driven conditions [4,8,23–28]. In these systems, free-energy differences are typically inferred via fluctuation relations such as the Jarzynski equality, yielding equilibrium state functions despite nonequilibrium driving. Moreover, the accessible charge states are restricted to $N = 0$ or 1 by large charging energies $E_C \gg k_B T$, limiting the Shannon entropy to $\ln 2$ and the accessible range of free-energy variation. Here, k_B is the Boltzmann constant and T is the temperature. In addition, since these systems are typically not operated under steady nonequilibrium driving, an experimental decomposition of heat into excess and housekeeping components has not yet been achieved, and would, in any case, remain limited by the two-state nature. Related studies in nonelectronic platforms such as colloidal beads and granular media have verified steady-state relations [29–31], but they also do not provide explicit heat decomposition or probe the multielectron dynamics.

In contrast, multielectron systems operating at $E_C \lesssim k_B T$ possess a large state space and allow strong nonequilibrium driving. While equilibrium electron-number distributions are Gaussian [32,33], nonequilibrium driving can induce non-Gaussian distortions, leading to qualitatively different entropy production and free-energy characteristics. This expanded state space enables simultaneous and pronounced variations

*Contact author: nishiguchi-katsuhiko-kr@ynu.ac.jp

Published by the American Physical Society under the terms of the Creative Commons Attribution 4.0 International license. Further distribution of this work must maintain attribution to the author(s) and the published article's title, journal citation, and DOI.

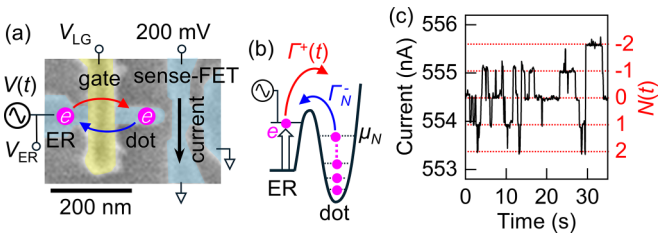


FIG. 1. (a) False scanning-electron-microscope image of the device for single-electron counting statistics. The constant ER voltage V_{ER} was 0.5 V. The details of the device structure are explained in Appendix D. (b) Energy band diagram between the ER and dot when the excess number of electrons in the dot is N. The Fermi energy of the ER is modulated by an ac signal $V(t)$ superimposed on V_{ER}. (c) Current flowing through the sense-FET without the ac signal. The sampling rate of the sense-FET was 20 Hz.

of excess and housekeeping heats, necessitating an analysis based on the full time-dependent probability distribution.

In this study, we experimentally quantify heat dissipation and Shannon entropy in a small dot with multielectron occupancy driven by an ac signal. Using single-electron counting statistics, we track the dynamics of many electrons in a device that mimics a dynamic random-access-memory (DRAM) cell. Although $E_C \lesssim k_B T$, the electron number remains a well-defined state variable. We decompose the total heat into housekeeping and excess components, reveal their quantitative relation to nonequilibrium free-energy generation and efficiency, and demonstrate how multielectron systems provide a direct thermodynamic framework connecting heat dissipation to electronic-device operation far from equilibrium.

II. EXPERIMENTAL SYSTEM

Figure 1(a) shows our device for single-electron counting statistics: The individual motion of single electrons traveling back and forth between an electron reservoir (ER) and the dot is monitored [34]. Since all measurements were carried out at room temperature, the electron motion originates not from tunneling events but from thermal hopping over an energy barrier under a gate [see Fig. 1(b)] [35]. These structures and principles are similar to conventional DRAMs, except that the dot in our device is very small (about 10 aF in capacitance), storing approximately 20 electrons. The electrons in the dot are counted with a field-effect transistor (FET), referred to as the sense-FET: The current flowing through the sense-FET increases/decreases in a steplike pattern when a single electron leaves/enters the dot, as shown in Fig. 1(c). From the step height caused by a single electron and the sense-FET's transconductance, the charging energy E_C for one electron stored in the dot was estimated to be 9.8 meV [34].

We control equilibrium and nonequilibrium states between the ER and the dot, hereafter defined as the ER-dot system, by modulating the Fermi energy of the ER [36]. In the equilibrium state, constant voltages are applied to the ER and gate, respectively. Since the energy barrier height controlled by the gate governs the transition rate of electrons surmounting the barrier considering Kramers' rate [37], the transition rate Γ_0 for an electron to enter the dot is constant, while the rate Γ_N^- for an electron to leave the dot is given by $\Gamma_0 \exp(\beta\mu_N)$[32], where $\mu_N = 2E_C(N - 0.5)$ is the chemical potential of the dot, N is the deviation from the average number of electrons in the dot at equilibrium [see Fig. 1(b)], and $\beta = (k_B T)^{-1}$ is the inverse temperature. These transition rates are estimated experimentally from $N(t)$, where $N(t)$ is the time evolution of N [Fig. 1(c)] [32]. Γ_0 is adjusted to be 0.1 Hz to ensure that the electron motion is slow enough to be precisely monitored.

The nonequilibrium state is induced by superimposing an ac voltage signal, $V(t) = S_{AC} \sin(\omega_{AC} t + \phi)$, on the constant ER voltage [36]. Here, S_{AC}, $\omega_{AC}/2\pi$, and ϕ are the amplitude, frequency, and phase of the ac signal. The ac signal changes the energy barrier for electrons in the ER by $-eV(t)$, and therefore the transition rate for entering the dot is modulated over time, $\Gamma^+(t) = \Gamma_0 \exp[-\beta eV(t)]$. In contrast, the escape rate $\Gamma_N^- = \Gamma_0 \exp(\beta\mu_N)$ remains unaffected. In this study, $\omega_{AC}/2\pi$ of 1 Hz larger than Γ_0 prevents electrons from following the ac signal and thus pushes the ER-dot system out of equilibrium. Detailed frequency dependence is discussed in Ref. [36] and Appendix A.

To perform statistical analysis, all measured quantities are evaluated as phase-averaged ensemble averages. In the experiment, the phase ϕ of the applied ac signal is randomized for each measurement, and the results are averaged over many repetitions. This procedure removes phase-dependent contributions and provides access to the intrinsic stochastic properties of the system.

A central quantity in our analysis is the time-dependent probability $\rho_N(t)$, which we obtain from the statistical analysis of repeated measurements. Here, $\rho_N(t)$ represents the probability that the dot contains an excess electron number N at time t. The probability distribution is obtained by converting the measured sense-FET current into $N(t)$ and averaging over the phase ensemble.

In the theoretical analysis, we assume that the phase ϕ is uniformly distributed. Under this assumption, all observables correspond to phase-averaged quantities, and the time-averaged driving voltage vanishes. This ensures direct consistency between experimental observables and the theoretical framework.

III. THEORETICAL FRAMEWORK

A. Master equation

The dynamics of the ER-dot system can be described by the following master equation:

$$\dot{\rho}_N(t) = \Gamma^+(t)\rho_{N-1}(t) - [\Gamma^+(t) + \Gamma_N^-]\rho_N(t) + \Gamma_{N+1}^-\rho_{N+1}(t), \quad (1)$$

where $\sum_{N=-\infty}^{\infty} \rho_N(t) = 1$. Throughout this paper, the dot notation $\dot{\square}$ represents the time derivative of $\square$.

The Fourier series expansion of the time-dependent quantities $\Gamma^+(t)$ and $\rho_N(t)$ provides a systematic framework to analyze the master equation and extract its dominant dynamics (see Appendix A). Based on this analysis, the time-dependent transition rate $\Gamma^+(t)$ can be approximated by its

time-averaged value,

$$\Gamma^+(t) \approx \overline{\Gamma^+} = \Gamma_0 I_0(\beta e S_{\rm AC}), \tag{2}$$

where $I_0(\square)$ is the modified Bessel function of the first kind.

Under this approximation, which effectively corresponds to a coarse-grained description over the driving period, the probability distribution $\rho_N(t)$ in the NESS can be approximated by a stationary distribution $\rho_N^{\rm SS}$, which takes a Gaussian form, as obtained from the Fourier analysis (see Appendix A):

$$\rho_N^{\rm SS} = Z^{-1} \exp[-\beta E_{\rm C}(N - \langle N_{\rm SS}\rangle)^2], \tag{3}$$

where

$$\langle N_{\rm SS}\rangle = \ln(\overline{\Gamma^+}/\Gamma_0)/(2\beta E_{\rm C}) \tag{4}$$

corresponds to the zero-frequency component in the Fourier expansion of $\langle N(t)\rangle$ in the NESS. Z is given by $\sum_{N=-\infty}^{\infty} \exp[-\beta E_{\rm C}(N - \langle N_{\rm SS}\rangle)^2]$.

The validity of these approximations will be examined by direct comparison with the experimental results presented in Sec. IV. This approach is further supported by previous studies on stochastic pumps [38], where similar approximations have been successfully applied to ac-driven systems with modulation faster than the experimental sampling rate, making it particularly suitable for the present system.

B. Heat dissipation rate for single-electron motion

Heat dissipation is estimated from individual electron motions between the ER and dot. When the excess electron number in the dot changes from N to $N+1$ or $N-1$, its heat dissipation Q_N^{+1} or Q_N^{-1}, respectively, is given by

$$Q_N^{\pm 1} = -(H_{N\pm 1} - H_N). \tag{5}$$

Here, H_N is the Hamiltonian when the number of excess electrons in the dot is N [26]: $H_N = E_{\rm C}(N - N_{\rm off})^2 - E_{\rm C}N_{\rm off}^2$, where $N_{\rm off} = -eV(t)/(2E_{\rm C})$. Consequently, Eq. (5) yields [see Fig. 1(b)]

$$Q_N^{+1} = -eV(t) - \mu_{N+1}, \tag{6}$$

$$Q_N^{-1} = eV(t) + \mu_N. \tag{7}$$

By multiplying Eqs. (6) and (7) by probability flows, the heat-dissipation rates for electrons entering and leaving the dot are given by

$$\langle \dot{Q}^+(t)\rangle = \sum_{N=-\infty}^{\infty} \rho_N(t)\Gamma^+(t)[-eV(t) - \mu_{N+1}], \tag{8}$$

$$\langle \dot{Q}^-(t)\rangle = \sum_{N=-\infty}^{\infty} \rho_N(t)\Gamma_N^-[eV(t) + \mu_N], \tag{9}$$

respectively. The total heat dissipation rate $\langle \dot{Q}_{\rm T}(t)\rangle$ is defined as $\langle \dot{Q}_{\rm T}(t)\rangle = \langle \dot{Q}^+(t)\rangle + \langle \dot{Q}^-(t)\rangle$.

Next, we consider heat dissipation in an NESS. $\rho_N(t)$ in the NESS relaxes to a Gaussian distribution $\rho_N^{\rm SS}$ given by Eq. (3). Given that μ_N, $\rho_N^{\rm SS}$, and Γ_N^- are time independent, that $\Gamma^+(t)$ is averaged over time, i.e., $\overline{\Gamma^+}$, and that the phase- or time-averaged $V(t)$ is zero, Eqs. (8) and (9) yield $\langle \dot{Q}^+(t)\rangle$ and $\langle \dot{Q}^-(t)\rangle$ in an NESS:

$$\langle \dot{Q}^{+{\rm SS}}(t)\rangle = -eV(t)\Gamma^+(t) - 2E_{\rm C}(\langle N_{\rm SS}\rangle + 0.5)\overline{\Gamma^+}, \tag{10}$$

$$\langle \dot{Q}^{-{\rm SS}}(t)\rangle = 2E_{\rm C}(\langle N_{\rm SS}\rangle + 0.5)\overline{\Gamma^+}. \tag{11}$$

Because the instantaneous dissipation depends on the phase of the ac drive, the term $eV(t)\Gamma^+(t)$ is left as a time-dependent quantity here, while its time-averaged form is given later (Appendix C). Consequently, $\langle \dot{Q}_{\rm T}(t)\rangle$ in an NESS becomes

$$\langle \dot{Q}_{\rm T}^{\rm SS}(t)\rangle = \langle \dot{Q}^{+{\rm SS}}(t)\rangle + \langle \dot{Q}^{-{\rm SS}}(t)\rangle = -eV(t)\Gamma^+(t). \tag{12}$$

Since $-e\Gamma^+(t)$ corresponds to electric current from the ER to the dot, Eq. (12) corresponds to the electric power dissipation or work rate to maintain the ER-dot system in the NESS.

C. Decomposition into excess and housekeeping heats

Excess heats $Q_{{\rm EX},N}^{+1}$ and $Q_{{\rm EX},N}^{-1}$ for an electron entering and leaving the dot when the excess electron number is N are given by [15]

$$\beta Q_{{\rm EX},N}^{\pm 1} = \ln\left(\frac{\rho_{N\pm 1}^{\rm SS}}{\rho_N^{\rm SS}}\right). \tag{13}$$

Substituting Eq. (3) into Eq. (13) gives

$$Q_{{\rm EX},N}^{+1} = 2E_{\rm C}\langle N_{\rm SS}\rangle - \mu_{N+1}, \tag{14}$$

$$Q_{{\rm EX},N}^{-1} = -2E_{\rm C}\langle N_{\rm SS}\rangle + \mu_N. \tag{15}$$

Housekeeping heats $Q_{{\rm HK},N}^{+1}$ and $Q_{{\rm HK},N}^{-1}$ for an electron entering and leaving the dot, respectively, at N follow

$$\begin{aligned}\beta Q_{{\rm HK},N}^{\pm 1} &= \ln\left[\frac{R(N\pm 1|N)}{R(N|N\pm 1)}\frac{\rho_N^{\rm SS}}{\rho_{N\pm 1}^{\rm SS}}\right] \\ &= \pm[-eV(t) - 2E_{\rm C}\langle N_{\rm SS}\rangle],\end{aligned} \tag{16}$$

where $R(y|x)$ is the transition rate for N to change from x to y. Consequently, Eqs. (6) and (7) are decomposed:

$$\begin{aligned}Q_N^{+1} =& [-eV(t) - 2E_{\rm C}\langle N_{\rm SS}\rangle] \\ &+ [2E_{\rm C}\langle N_{\rm SS}\rangle - \mu_{N+1}],\end{aligned} \tag{17}$$

$$\begin{aligned}Q_N^{-1} =& [eV(t) + 2E_{\rm C}\langle N_{\rm SS}\rangle] \\ &+ [-2E_{\rm C}\langle N_{\rm SS}\rangle + \mu_N].\end{aligned} \tag{18}$$

The first and second square brackets on the right-hand sides correspond to housekeeping and excess heats, respectively.

Equations (17) and (18) clarify the connection between the decomposition at the level of single-electron transitions and the averaged heat dissipation rates in Eqs. (10), (11), and (12). Within this correspondence, the physical origin of the factor of 1/2 in Eqs. (10) and (11) can be traced back to the offset in the electrochemical potential $\mu_{N+1} = 2E_{\rm C}(N + 0.5)$, which reflects the discrete nature of charge transitions. Upon ensemble averaging, this offset gives rise to a constant contribution that contributes to the excess heat in the thermodynamic decomposition. These expressions also provide a direct route to experimentally reconstruct $Q_{\rm EX}$ and $Q_{\rm HK}$ from the time evolution of N, as discussed below.

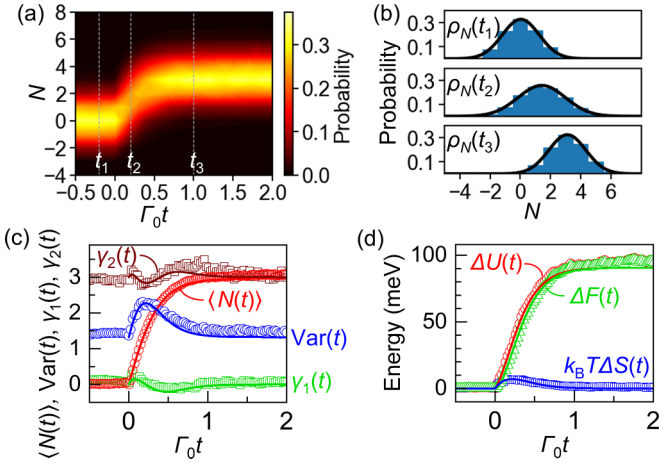


FIG. 2. (a) Contour plot of the $\rho_N(t)$ distributions from an equilibrium state to an NESS. The ac signal with amplitude S_{AC} of 100 mV was applied at $t = 0$. Experimental data were averaged over 3000 repetitions. (b) $\rho_N(t)$ distributions at t_1, t_2, and t_3 depicted in panel (a). The solid lines are the Gaussian fits to the experimental results. (c) Transient characteristics of the average $\langle N(t)\rangle$, variance Var(t), skewness $\gamma_1(t)$, and kurtosis $\gamma_2(t)$ of $\rho_N(t)$. (d) Transient characteristics of the deviations of the internal energy $\Delta U(t)$, free energy $\Delta F(t)$, and Shannon entropy $k_B T \Delta S(t)$ from their initial values at $t = 0$. Open marks are the experimental data, and the solid lines are the numerical results of the master equation.

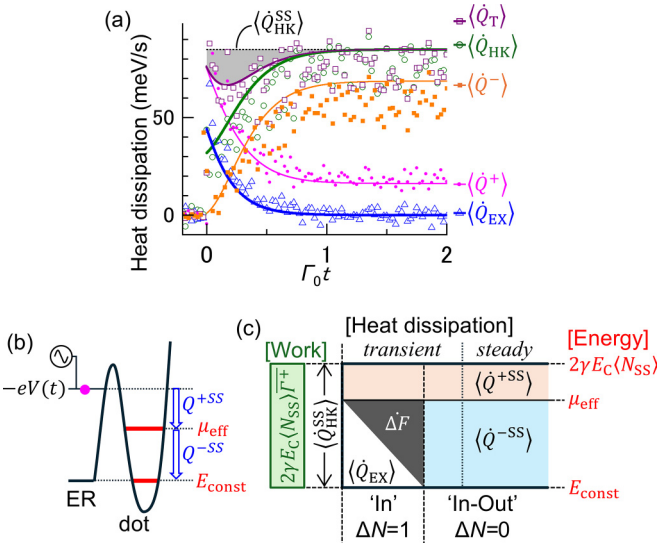


FIG. 3. (a) $\langle \dot{Q}_T\rangle$ and its decomposition into $\langle \dot{Q}_{EX}\rangle$, $\langle \dot{Q}_{HK}\rangle$, $\langle \dot{Q}^+\rangle$, and $\langle \dot{Q}^-\rangle$. For brevity, the explicit time argument (t) of these quantities is omitted. Q_{EX} and Q_{HK} are evaluated from $N(t)$ [Fig. 1(c)] using Eqs. (14)–(16) together with the experimentally determined transition rates. The steady-state quantities ρ_N^{SS} and $\langle N_{SS}\rangle$ are obtained from the experimental data in the NESS (Fig. 2). The corresponding heat dissipation rates are then derived by taking the time derivative. Scatter points are experimental averages over 3000 repetitions, and solid lines are numerical results from the master equation. The gray region shows $\langle \dot{Q}_{HK}^{SS}\rangle - \langle \dot{Q}_T\rangle$. $S_{AC} = 100$ mV. (b) Energy band diagram of the ER-dot system. Q^{+SS} and Q^{-SS} correspond to heat dissipation when one electron enters and leaves, respectively, the dot in the NESS [see Eqs. (8) and (9)]. (c) Schematic representation of heat dissipation, free-energy generation, and work. The left and right vertical axes represent these rates and the corresponding energy levels (in red), respectively. The horizontal axis indicates "In" and "In-Out" events, in which N increases by one and in which the same number of electrons enter and leave the dot, respectively. Although these events occur stochastically, they are grouped into two categories. The shaded areas represent the total heat dissipated in each process.

IV. DYNAMICS OF THE PROBABILITY DISTRIBUTION AND ENTROPY PRODUCTION

Figures 2(a) and 2(b) show the distributions of $\rho_N(t)$ over time t when an ac signal was applied at $t = 0$. To characterize equilibrium and nonequilibrium states of the ER-dot system, we consider the average $\langle N(t)\rangle$, given by $\sum_{N=-\infty}^{\infty} \rho_N(t) N$, and the variance Var($t$), given by $\sum_{N=-\infty}^{\infty} \rho_N(t)[N - \langle N(t)\rangle]^2$, of N at time t, which are summarized in Fig. 2(c).

Before the ac signal is applied, the system is in equilibrium: $\rho_N(t)$ follows a Gaussian distribution with a mean $\langle N(t)\rangle$ of zero and a variance Var(t) given by $(2\beta E_C)^{-1}$ as shown by the $\rho_N(t_1)$ distribution in Fig. 2(b), meaning the electron motion between the ER and the dot is thermally activated [32]. After the ac signal is applied, the dynamic change in the ER voltage causes a temporal disruption of the detailed balance condition, placing the ER-dot system in nonequilibrium, which generates entropy production as discussed below. As shown in Fig. 2(b), the bell-shaped distribution of $\rho_N(t)$ shifts positively in N and $\langle N(t)\rangle$ increases over time. Meanwhile, Var(t) initially increases and then decreases. During this interval, the skewness $\gamma_1(t)$ and kurtosis $\gamma_2(t)$ of the $\rho_N(t_2)$ distribution deviate from 0 and 3, respectively, meaning that $\rho_N(t_2)$ deviates from a Gaussian distribution. Finally, after $t \sim 1/\Gamma_0$, the distribution $\rho_N(t_3)$ stabilizes to a Gaussian distribution: Its average $\langle N(t)\rangle$ and variance Var(t) are given by $\langle N_{SS}\rangle$ and $(2\beta E_C)^{-1}$, respectively. The transition rate for electrons entering the dot balances with the rate of escaping electrons, meaning the local detailed balance holds between the ER and the dot, and the system reaches an NESS [36]. These features mean that $\rho_N(t_3)$ can be represented by the stationary probability distribution ρ_N^{SS} given by Eq. (3) derived from the Fourier analysis of the master equation (also see Appendix A).

As shown in Fig. 2(c), the dynamic features of $\rho_N(t)$ are traced well by the numerical results of the master equation using the Fourier series expansion, implying that the approximation by such Fourier analysis described in Sec. III A is valid for the ER-dot system driven by an ac signal with a frequency higher than Γ_0 (Figs. 2–4).

Next, we discuss the entropy production during the dynamic ER-dot system. The entropy production in nonequilibrium can be expressed as the sum of the change in the Shannon entropy $S(t)$ and the heat dissipation. First, we discuss $S(t)$ and its change $\Delta S(t)$ given by $-\sum_{N=-\infty}^{\infty} \rho_N(t) \ln \rho_N(t)$ and $S(t) - S(0)$, respectively. As shown in Figs. 2(c) and 2(d), during the state transition from the equilibrium state to the NESS, Var(t) increases, leading to an increase in $\Delta S(t)$. In the NESS, Var(t) returns to its initial value $(2\beta E_C)^{-1}$, as confirmed at various values of ω_{AC} and S_{AC} in Ref. [36], implying $\Delta S(t) = 0$. Since $k_B T \Delta S(t)$ is much

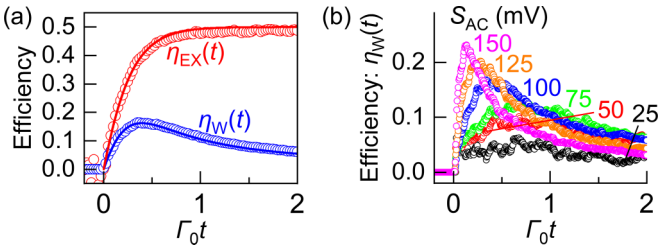


FIG. 4. (a) Change in efficiencies η_{EX} and η_W. $S_{AC} = 100$ mV. Open circles are experimental results averaged over 30 000 repetitions. The solid lines are theoretical results obtained from the master equation. (b) S_{AC} dependencies of η_W. Each curve is averaged over 250 repetitions.

smaller than the heat dissipation explained in the next section, we consider the entropy production to be dominated by heat dissipation in the present system.

Additionally, $\Delta S(t)$ is sufficiently small that the change in the internal energy $\Delta U(t)$, given by $\sum_N E_C N^2 \rho_N(t)$, is close to the free-energy change $\Delta F(t)$ [see Fig. 2(c)], since $\Delta F(t) = \Delta U(t) - k_B T \Delta S(t)$ [13]. This behavior can be understood from the near-Gaussian form of $\rho_N(t)$: The skewness $\gamma_1(t)$ and kurtosis $\gamma_2(t)$ remain close to 0 and 3, respectively [Fig. 2(c)], indicating only a small deviation from a Gaussian distribution. Under this condition, $\Delta F(t)$ can be approximated as $E_C \langle N(t) \rangle^2$ (see Appendix A). Consistent with this approximation, as shown in Fig. 2(d), $\Delta F(t)$ increases monotonically and saturates at $E_C \langle N_{SS} \rangle^2$ in the NESS.

V. EXPERIMENTAL DECOMPOSITION OF HEAT DISSIPATION

We next evaluate the heat dissipation in the dynamic ER-dot system and examine its decomposition based on the theoretical framework introduced in Sec. III C.

We first present the experimental results. Figure 3(a) shows the time evolution of $\langle \dot{Q}_T(t) \rangle$ and its decomposition into $\langle \dot{Q}_{EX}(t) \rangle$ and $\langle \dot{Q}_{HK}(t) \rangle$. Q_{EX} and Q_{HK} are experimentally reconstructed from $N(t)$ using Eqs. (14)–(16) together with the measured transition rates. At $t = 0$, $\langle \dot{Q}_{EX}(t) \rangle$ is maximal. Then, it monotonically decreases and becomes zero in the NESS. In contrast, $\langle \dot{Q}_{HK}(t) \rangle$ is already finite in the transient regime and gradually approaches a constant value $\langle \dot{Q}^{SS}_{HK} \rangle$.

The experimental analysis on $\langle \dot{Q}_T(t) \rangle$ and $\langle \dot{Q}^{SS}_{HK} \rangle$, combined with the numerical analysis using the master equation of Eq. (1), leads to the following energy balance relation:

$$\int_0^{\tau_{SS}} \langle \dot{Q}_T(t) \rangle dt + \Delta F_{SS} = \int_0^{\tau_{SS}} \langle \dot{Q}^{SS}_{HK} \rangle dt, \tag{19}$$

which connects the transient heat dissipation to the free energy ΔF_{SS} in the NESS.

To understand the physical origin of this relation, we now consider the microscopic energy or heat flows. Figure 3(b) provides a schematic overview of the heat dissipation processes. In the NESS, Eqs. (10) and (11) describe the heat flow required to maintain the steady state. The term $2E_C \langle N_{SS} \rangle$ can be interpreted as an effective chemical potential μ_{eff}, which characterizes the energy level of the dot. Equation (10) represents the heat dissipation associated with an electron entering the dot from the ER with energy $-eV(t)$ [see Q^{+SS} shown in Fig. 3(b)], while Eq. (11) describes the dissipation when an electron in the dot returns to the ER with the reference energy E_{const} (see Q^{-SS}). E_{const} corresponds to the Fermi energy of the ER in the absence of the ac signal. These kinds of heat dissipation stem from the work applied to the system, i.e., the time-dependent potential $-eV(t)$.

These considerations on heat flows are extended to those in the transition state before the NESS by classifying stochastic events into two types: "In" events and "In-Out" events [see Fig. 3(c)]. "In" events in which an electron only enters the dot contribute the increase in $\langle N(t) \rangle$ from zero to $\langle N_{SS} \rangle$. An electron entering the dot dissipates heat given by $Q_N^{+1} = [-eV(t) - \mu_{eff}] + (\mu_{eff} - \mu_{N+1})$ [Eq. (6)]. The first term of the right-hand side corresponds to the housekeeping component given by Eq. (16) and Q^{+SS} as shown in Fig. 3(b). The second term corresponds to the excess component given by Eq. (14). The sum of this excess component, i.e., $\sum_{N=0}^{\langle N_{SS} \rangle - 1} (\mu_{eff} - \mu_{N+1})$, during the "In" events is equal to $E_C \langle N_{SS} \rangle^2 = \Delta F_{SS}$. In contrast, since the work $-eV(t)$ is applied to the system, the remaining energy, $-eV(t) - Q_N^{+1} = \mu_{N+1}$, is stored in the dot as the free energy, and the sum of μ_N during the "In" events becomes ΔF_{SS}. The agreement between these two values resembles the relationship between free energy and heat dissipation when charging a capacitor with a direct-constant (dc) voltage. In other words, the minimum energy required to accumulate free energy corresponds to the excess heat—the minimum energy required for the state transition.

In the "In-Out" events, the number of electrons entering and leaving the dot is balanced, and the net change ΔN in N is zero. In this case, for each value of N, an electron entering the dot dissipates $Q_N^{+1} = [-eV(t) - \mu_{eff}] + (\mu_{eff} - \mu_{N+1})$, while an electron leaving dissipates $Q_{N+1}^{-1} = [eV(t) + \mu_{eff}] + (-\mu_{eff} + \mu_{N+1})$. Here, the second terms correspond to the excess components and cancel between the "In" and "Out" processes. In contrast, the first terms represent the housekeeping contributions, which explicitly depend on $V(t)$ and therefore do not cancel at each instant. However, when taking the time average over the stochastic transitions, the contribution from $V(t)$ in Q_{N+1}^{-1} vanishes because the time average of $V(t)$ is zero and the transition rates for electron leaving the dot are not correlated with $V(t)$ over a full period. Therefore, when we consider the events of entering and leaving the dot as a set, we can regard $\langle \dot{Q}_N^{+1} \rangle$ and $\langle \dot{Q}_{N+1}^{-1} \rangle$ as $\langle \dot{Q}^{+SS} \rangle$ and $\langle \dot{Q}^{-SS} \rangle$ given by Eqs. (10) and (11), respectively. It should be noted that these considerations are valid for the transient and steady states as shown in Fig. 3(c).

Consequently, the total heat dissipation satisfies Eq. (19). Here, the difference between the two terms corresponds to the free energy stored in the dot,

$$\Delta F_{SS} = E_C \langle N_{SS} \rangle^2 = \langle N_{SS} \rangle \mu_{eff} - \sum_{N=0}^{\langle N_{SS} \rangle - 1} (\mu_{eff} - \mu_{N+1}), \tag{20}$$

which arises from the accumulated excess contributions during the "In" events. Using $\langle \dot{Q}_T(t) \rangle = \langle \dot{Q}_{EX}(t) \rangle + \langle \dot{Q}_{HK}(t) \rangle$ together with Eq. (19), we obtain an alternative expression for

the free energy,

$$\Delta F_{\rm SS} = \frac{1}{2}\int_0^{\tau_{\rm SS}} \left[\langle \dot{Q}_{\rm HK}^{\rm SS}\rangle - \langle \dot{Q}_{\rm HK}(t)\rangle\right] dt. \tag{21}$$

This relation shows that the free energy can be quantified from the deviation of the housekeeping heat from its steady-state value during the transient dynamics.

Finally, we examine the consistency of the above heat decomposition from a thermodynamic viewpoint. In a driven system, the heat dissipation must be balanced by the work continuously supplied to the system. Equation (12) describes the work rate on the ER-dot system [28]. Its time average is given by

$$\int_0^{2\pi/\omega_{\rm AC}} [-eV(t)\Gamma(t)^+] dt = 2\gamma E_{\rm C}\langle N_{\rm SS}\rangle \overline{\Gamma^+}, \tag{22}$$

where γ monotonically decreases with an increase in $\beta S_{\rm AC}$. Specifically, γ approximates 1 if $\beta e S_{\rm AC} \gg 1$ and γ approximates 2 if $\beta e S_{\rm AC} \ll 1$ (see Appendix C). This result confirms that the continuous energy input from the ac drive accounts for the sustained housekeeping heat dissipation in both transient and steady regimes.

VI. EFFICIENCY AND ITS LIMIT

Having established the decomposition of heat dissipation and the associated energy balance, we now turn to the efficiency of energy conversion in the driven ER-dot system, based on the second law for excess heat and the energy balance established above.

The correlation between $\langle \dot{Q}_{\rm EX}(t)\rangle$ and $\Delta F(t)$ provides a thermodynamic basis for defining the efficiency $\eta_{\rm EX}(t)$ through the second law for excess heat. Hatano and Sasa [15] showed $\langle Q_{\rm EX}(t)\rangle + k_B T \Delta S(t) \geqslant 0$. Using the nonequilibrium free-energy relation $\Delta F(t) = \Delta U(t) - k_B T \Delta S(t)$, we obtain $\langle Q_{\rm EX}(t)\rangle + \Delta U(t) \geqslant \Delta F(t)$. This inequality naturally suggests defining an efficiency that quantifies how much of the total energy input is converted into free energy:

$$\eta_{\rm EX}(t) = \frac{\Delta F(t)}{\langle Q_{\rm EX}(t)\rangle + \Delta U(t)}. \tag{23}$$

As shown in Fig. 4(a), $\eta_{\rm EX}(t)$ increases and then converges to a steady-state value. Since $\Delta F(t) \approx \Delta U(t)$ and $\langle Q_{\rm EX}^{\rm SS}\rangle = \Delta F_{\rm SS}$, the upper bound of $\eta_{\rm EX}(t)$ is 0.5 in the NESS. This result implies that, in the NESS, at most half of the input energy can be converted into free energy, while the remaining half is inevitably dissipated. Although the microscopic mechanisms differ, this balance is reminiscent of classical capacitor charging, where half of the supplied energy is stored and half is inevitably dissipated as explained above [see Fig. 3(c)].

These understandings based on Fig. 3(c) also offer information on the energetic efficiency for free-energy generation [39]:

$$\eta_{\rm W}(t) = \frac{\Delta F(t)}{[\langle Q_{\rm T}(t)\rangle + \Delta U(t)]}, \tag{24}$$

where $\langle Q_{\rm T}(t)\rangle = \int_0^t \langle \dot{Q}_{\rm T}(t')\rangle dt'$. The denominator corresponds to the total input work, as it includes both the accumulated heat dissipation and the stored internal energy. Figure 4(a) shows the transient characteristics of $\eta_{\rm W}(t)$: $\eta_{\rm W}(t)$ rises, peaks, and then gradually decreases over time unlike $\eta_{\rm EX}(t)$, which monotonically approaches 0.5. Additionally, increasing $S_{\rm AC}$ raises the peak values of $\eta_{\rm W}(t)$, which reach up to 0.25 at 150 mV in experiments as shown in Fig. 4(b).

To characterize $\eta_{\rm W}(t)$, we consider the efficiency $\eta_{\rm SS}$ when the system reaches the NESS at $t = \tau_{\rm SS}$. Since $\Delta F(\tau_{\rm SS})$ is its maximum $\Delta F_{\rm SS}$ given by $E_{\rm C}\langle N_{\rm SS}\rangle^2$ and nearly equal to $\Delta U(\tau_{\rm SS})$, Eq. (19) gives

$$\eta_{\rm SS} = \frac{E_{\rm C}\langle N_{\rm SS}\rangle^2}{\int_0^{\tau_{\rm SS}} \langle \dot{Q}_{\rm HK}^{\rm SS}\rangle dt}. \tag{25}$$

We define $\tau_{\rm th}$ as the moment when $\langle N(t)\rangle$ reaches a threshold value of $a\langle N_{\rm SS}\rangle$, where $0 < a < 1$ (see Appendix B). Since $\langle \dot{Q}_{\rm HK}^{\rm SS}\rangle = 2\gamma E_{\rm C}\langle N_{\rm SS}\rangle \overline{\Gamma^+}$ as explained above, $\eta_{\rm SS}$ is given by

$$\eta_{\rm SS} \sim -\frac{(\beta e S_{\rm AC})^2}{16\ln(1-a)} \quad \text{if } \beta e S_{\rm AC} \ll 1, \tag{26}$$

$$\eta_{\rm SS} \sim \frac{1}{a+1} = 0.5 \quad \text{if } \beta e S_{\rm AC} \gg 1 \text{ and } a = 1. \tag{27}$$

The independence of Eqs. (26) and (27) from $E_{\rm C}$ highlights a universal scaling behavior: The maximum efficiency is determined solely by the driving strength $\beta S_{\rm AC}$, which quantifies how far the system is driven from equilibrium. When $\beta S_{\rm AC} \gg 1$, the efficiency $\eta_{\rm SS}$ approaches its upper bound of 0.5 in the NESS. This trend is counterintuitive: A larger $S_{\rm AC}$ drives the system further from equilibrium, and one would normally expect stronger irreversibility to reduce efficiency. This seemingly anomalous increase in efficiency arises because a larger $S_{\rm AC}$ substantially suppresses the housekeeping heat, as illustrated in Fig. 3(c). An increase in $S_{\rm AC}$ reduces the parameter γ, making $2\gamma E_{\rm C}\langle N_{\rm SS}\rangle$ close to $\mu_{\rm eff}$, which in turn decreases the housekeeping component of $\langle \dot{Q}^{+\rm SS}(t)\rangle$. Simultaneously, a larger $S_{\rm AC}$ shortens the approach time $\tau_{\rm th}$ [see Eq. (B10) in Appendix B], thereby reducing $\langle \dot{Q}^{+}(t)\rangle$ and $\langle \dot{Q}^{-\rm SS}(t)\rangle$, i.e., $\langle Q_{\rm HK}(t)\rangle$, before the NESS is reached. In other words, $\langle Q_{\rm T}(t)\rangle \approx \langle Q_{\rm EX}(t)\rangle$ until the NESS, implying that $\eta_{\rm W}(t)$ becomes nearly identical to $\eta_{\rm EX}(t)$. In contrast, when $\beta S_{\rm AC} \ll 1$, the system approaches the NESS slowly (large $\tau_{\rm SS}$) and γ increases toward 2, enhancing $\langle Q_{\rm HK}(t)\rangle$ and thereby lowering the efficiency.

VII. SUMMARY

We experimentally decomposed the heat dissipation of a multielectron dot into excess and housekeeping components and revealed that free-energy generation is fundamentally limited by their competition. Our analysis shows that the efficiency can approach the upper bound of 0.5 under strong nonequilibrium driving, independent of device-specific parameters. By introducing an effective time-averaged transition rate for ac-driven dynamics, we obtain a compact description of periodically driven stochastic electron systems and a quantitative thermodynamic framework linking heat decomposition to free-energy generation. These results enable systematic evaluation of performance limits in electronic devices operated far from equilibrium.

ACKNOWLEDGMENTS

The authors thank Yasuhiko Tokura in Tsukuba University for valuable support on the theory. They also thank Keiji Saito

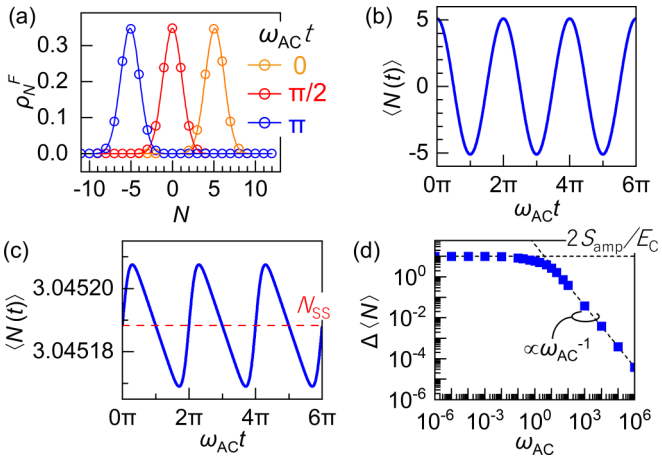


FIG. 5. (a) $\rho_N^F(t)$ at different time in the NESS. Open circles are given by Eq. (1) into which Eqs. (A1) and (A2) are substituted. The solid lines are Gaussian curves fitted to the open circles. Change in $\langle N(t)\rangle$ when (b) $\omega_{AC}/2\pi = 10^{-6}\Gamma_0$ and (c) $\omega_{AC}/2\pi = 10^{6}\Gamma_0$. (d) ω_{AC} dependence of $\Delta\langle N\rangle$, which is a peak-to-peak value of $\langle N(t)\rangle$ over time.

and Tan Van Vu in Kyoto University for fruitful discussion. This work was supported by the Japan Society for the Promotion of Science (JSPS) KAKENHI Grant No. JP26H02150.

DATA AVAILABILITY

The data that support the findings of this article are not publicly available. The data are available from the authors upon reasonable request.

APPENDIX A: SOLUTION OF MASTER EQUATION

When an ac signal is applied, the ER-dot system is described by the master equation given by Eq. (1). Since this ac signal oscillating with a frequency of $\omega_{AC}/2\pi$ is estimated to bring the periodicity to $\Gamma^{+}(t)$ and $\rho_N(t)$, we applied the Fourier series expansion to them, respectively:

$$\Gamma^{+(F)}(t)/\Gamma_0 = \exp[A\cos(\omega_{AC}t)] \sim I_0(A) + 2\sum_{k=1}^{K} I_k(A)\cos(k\omega_{AC}t), \tag{A1}$$

$$\rho_N^F(t) = \frac{p_0^{(N)}(t)}{2} + \sum_{l=1}^{K}\left[p_l^{(N)}(t)\cos(l\omega_{AC}t) + q_l^{(N)}(t)\sin(l\omega_{AC}t)\right]. \tag{A2}$$

$I_k(A) = 2/T_{AC}\int \exp[A\cos(\omega_{AC}t)]\cos(2k\pi/T_{AC})dt$ is the modified Bessel function of the first kind of order k, where $A = \beta e S_{AC}$ and $T_{AC} = 2\pi/\omega_{AC}$. K of 12 makes $\Gamma^{+(F)}(t)$ sufficiently close to $\Gamma^{+}(t)$. By substituting Eqs. (A1) and (A2) into Eq. (1), $\rho_N^F(t)$ is derived numerically.

When $\omega_{AC}/2\pi \ll \Gamma_0$, instantaneous distribution of $\rho_N^F(t)$ changes over time, keeping Gaussian distribution, and its average $\langle N(t)\rangle = \Sigma_N N\rho_N^F(t)$ changes periodically following the ac signal [Figs. 5(a) and 5(b)]. These features are natural because the ER voltage changes slowly enough for the system to follow it quasistatically.

When $\omega_{AC}/2\pi \gg \Gamma_0$ in an NESS, temporal change in $\rho_N^F(t)$ is too small to be distinguishable as shown in Fig. 5(c) depicting that $\langle N(t)\rangle$ fluctuates by about 10 ppm. This fluctuation decreases inversely proportional to ω_{AC} when $\omega_{AC}/2\pi \gg \Gamma_0$ as shown in Fig. 5(d). It should be noted that time average of this $\langle N(t)\rangle$ is the same as $\langle N_{SS}\rangle = \ln[I_0(A)]/2\beta E_C$. This $\langle N(t)\rangle$ fluctuation and its time average can be explained as follows.

The master equation, Eq. (1), is divided into the time-independent term and the $\cos(m\omega_{AC}t)$ and $\sin(m\omega_{AC}t)$ components:

$$0 = I_0(A)\frac{p_0^{(N-1)}}{2} + \sum_{l=1}^{K} I_l(A)p_l^{(N-1)} - \left[I_0(A) + e^{2\beta E_C(N-1/2)}\right]\frac{p_0^{(N)}}{2} - \sum_{l=1}^{K} I_l(A)p_l^{(N)} + e^{2\beta E_C(N+1/2)}\frac{p_0^{(N+1)}}{2}, \tag{A3}$$

$$\begin{aligned} m\omega_{AC}q_m^{(N)} = {} & I_0(A)p_m^{(N-1)} + I_m(A)p_0^{(N-1)} + \sum_{l=1}^{m-1} I_{m-l}(A)p_l^{(N-1)} + \sum_{l=1}^{K} I_{m+l}(A)p_l^{(N-1)} \\ & + \sum_{l=m+1}^{K} I_{l-m}(A)p_l^{(N-1)} - I_m(A)p_0^{(N)} - \left[I_0(A) + e^{2\beta E_C(N-1/2)}\right]p_m^{(N)} - \sum_{l=1}^{m-1} I_{m-l}(A)p_l^{(N)} \\ & - \sum_{l=1}^{K} I_{m+l}(A)p_l^{(N-1)} - \sum_{l=m+1}^{K} I_{l-m}(A)p_l^{(N-1)} + e^{2\beta E_C(N+1/2)}p_m^{(N+1)}, \end{aligned} \tag{A4}$$

$$\begin{aligned} m\omega_{AC}p_m^{(N)} = {} & I_0(A)q_m^{(N-1)} + \sum_{l=1}^{m-1} I_{m-l}(A)q_l^{(N-1)} - \sum_{l=1}^{K} I_{m+l}(A)q_l^{(N-1)} + \sum_{l=m+1}^{K} I_{l-m}(A)q_l^{(N-1)} \\ & - \left[I_0(A) + e^{2\beta E_C(N-1/2)}\right]q_m^{(N)} - \sum_{l=1}^{m-1} I_{m-l}(A)q_l^{(N)} - \sum_{l=1}^{K} I_{m+l}(A)q_l^{(N)} - \sum_{l=m+1}^{K} I_{l-m}(A)q_l^{(N)} \\ & + e^{2\beta E_C(N+1/2)}q_m^{(N+1)}. \end{aligned} \tag{A5}$$

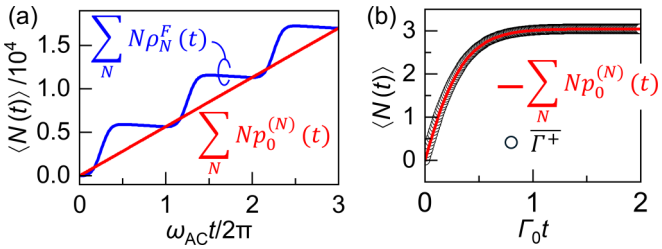


FIG. 6. Transient characteristics of $\langle N(t)\rangle$ over (a) a short time and (b) a long time span. In (a), periodic oscillations due to the ac signal and the dc component are both shown. $\omega_{AC}/2\pi = 10^6\Gamma_0$. Open circles in panel (b) show transient characteristics in the simplified model in the assumption that the transition rate for electrons entering the dot changes from Γ_0 to $\overline{\Gamma^+}$ at $t = 0$.

The normalizing condition is also divided into

$$1 = \sum_n p_0^{(n)}, \tag{A6}$$

$$0 = \sum_n p_m^{(n)}, \tag{A7}$$

$$0 = \sum_n q_m^{(n)}. \tag{A8}$$

Equations (A4) and (A5) imply that when $\omega_{AC}/2\pi \gg \Gamma_0$, $p_0^{(n)}$ must be much larger than $p_m^{(n)}$ and $q_m^{(n)}$ because the left parts of equations are proportional to ω_{AC}. In fact, fluctuation of $\langle N(t)\rangle$ decreases inversely proportional to ω_{AC} as shown in Fig. 5(d), which means that $p_m^{(n)}$ and $q_m^{(n)}$ are negligible. In this case, Eq. (A3) can be simplified to

$$0 = I_0(A)\frac{p_0^{(N-1)}}{2} - \left[I_0(A) + e^{2\beta E_C(N-1/2)}\right]\frac{p_0^{(N)}}{2} + e^{2\beta E_C(N+1/2)}\frac{p_0^{(N+1)}}{2}. \tag{A9}$$

Equation (A9) implies the time-independent master equation and gives $\Gamma^+(t) \sim \overline{\Gamma^+} = \Gamma_0 I_0(A)$, $\langle N_{SS}\rangle = \ln[I_0(A)]/2\beta E_C$, and

$$\Gamma^+(t) \sim \overline{\Gamma^+} = \Gamma_0 I_0(A), \tag{A10}$$

$$\langle N_{SS}\rangle = \ln[I_0(A)]/2\beta E_C. \tag{A11}$$

These features provide that

$$p_0^{(N)} = \rho_N^{SS} = \sqrt{\frac{\beta E_C}{\pi}}\exp[-\beta E_C(N - \langle N_{SS}\rangle)^2], \tag{A12}$$

implying that the variance of $\rho_N^F(t)$ is also approximated to $(2\beta E_C)^{-1}$. It was confirmed that these simplified parameters trace experimental results well [36].

Next, we consider transient characteristics from the equilibrium to the NESS. After the ac signal is applied, $\langle N(t)\rangle$ given by $\Sigma_N N\rho_N^F(t)$ increases with periodic oscillations, while $\langle N(t)\rangle$ given by $\Sigma_N Np_0^{(N)}(t)$ increases monotonically [Fig. 6(a)]. The discrepancy between them is small enough so that the transient characteristics can be represented by $\Sigma_N Np_0^{(N)}(t)$, i.e., dc part of the Fourier series expansion of Eq. (A2).

These features after and before the NESS imply that probability density can be represented by the dc part of the Fourier series expansion and thus that Γ^+ is represented by the dc part of $\Gamma^{+(F)}$, i.e., $\Gamma_0 I_0(A) = \overline{\Gamma^+}$. When we solve the master equation given by Eq. (1) in the assumption that Γ_0 is changed to $\overline{\Gamma^+}$ at $t = 0$, the derived transient characteristics of $\langle N(t)\rangle$ show good agreement with those of $\Sigma_N Np_0^{(N)}(t)$ as shown in Fig. 6(b), which enables us to use $\overline{\Gamma^+}$ for the theoretical analysis of the master equation in the main text.

Considering transient characteristics of the probability distribution $\rho_N(t)$, $\Delta F(t)$ can also be approximated. $U(t)$ is given by $\Sigma_N E_C N^2\rho_N(t)$. Since $\rho_N(t)$ has skewness and kurtosis close to zero and three, respectively, as shown in Fig. 2(c), it can be approximated to a Gaussian distribution given by $Z^{-1}\exp[-(N - \langle N(t)\rangle)^2/2\mathrm{Var}(t)]$, where $\mathrm{Var}(t)$ is time-dependent variance of $\rho_N(t)$. This approximation gives $U(t) = E_C\langle N(t)\rangle^2 + E_C\mathrm{Var}(t)$ and

$$\Delta U(t) = U(t) - U(0) = E_C\langle N(t)\rangle^2 + \frac{k_BT}{2}\left[\frac{\mathrm{Var}(t)}{\mathrm{Var}(0)} - 1\right]. \tag{A13}$$

Here, we use $\langle N(0)\rangle = 0$. Similarly, $S(t) = \Sigma_N\rho_N(t)\ln\rho_N(t)$ gives

$$\Delta S(t) = S(t) - S(0) = \tfrac{1}{2}[\ln\mathrm{Var}(t) - \ln\mathrm{Var}(0)]. \tag{A14}$$

Using Eqs. (A13) and (A14) gives

$$\Delta F(t) = \Delta U(t) - k_BT\Delta S(t) = E_C\langle N(t)\rangle^2 + \frac{k_BT}{2}\left[\frac{\mathrm{Var}(t)}{\mathrm{Var}(0)} - 1 - \ln\frac{\mathrm{Var}(t)}{\mathrm{Var}(0)}\right] \sim E_C\langle N(t)\rangle^2 + \frac{k_BT}{2}\left[\frac{1}{2}X(t)^2 + \mathcal{O}[X(t)]^3\right], \tag{A15}$$

where $X(t) = \mathrm{Var}(t)/\mathrm{Var}(0) - 1$. The second term proportional to k_BT is significantly smaller than the leading term $E_C\langle N(t)\rangle^2$. Consequently, the free-energy difference $\Delta F(t)$ can be approximated as $\Delta F(t) \approx E_C\langle N(t)\rangle^2$.

APPENDIX B: TRANSIENT CHARACTERISTICS UNTIL AN NESS

The transient characteristics of $\langle N(t)\rangle$ is given by [36]

$$\langle N(t)\rangle = \frac{\langle N_{SS}\rangle}{\ln(\overline{\Gamma^+}/\Gamma_0)} \times \ln\left[\frac{\overline{\Gamma^+}/\Gamma_0}{1 + (\overline{\Gamma^+}/\Gamma_0) - 1)\exp(-2\beta E_C\overline{\Gamma^+}t)}\right]. \tag{B1}$$

The moment τ_{th} when $\langle N(t)\rangle$ reaches a threshold value of $a\langle N_{SS}\rangle$, where $0 < a < 1$, is given by

$$\tau_{th} = \frac{\langle N_{SS}\rangle}{\overline{\Gamma^+}}\frac{1}{\ln(\overline{\Gamma^+}/\Gamma_0)}\ln\left[\frac{\overline{\Gamma^+}/\Gamma_0 - 1}{(\overline{\Gamma^+}/\Gamma_0)^{1-a} - 1}\right]. \tag{B2}$$

When $1/(1-a) \in N$,

$$\ln\left[\frac{\overline{\Gamma^+}/\Gamma_0 - 1}{(\overline{\Gamma^+}/\Gamma_0)^{1-a} - 1}\right] = \ln\left[\sum_{i=0}^{\frac{1}{1-a}-1}\left(\frac{\overline{\Gamma^+}}{\Gamma_0}\right)^{(1-a)i}\right]. \tag{B3}$$

From Appendix A,

$$\overline{\Gamma^+} = \frac{\omega_{\rm AC}}{2\pi}\int_0^{2\pi/\omega_{\rm AC}} \Gamma_0 \exp[\beta e S_{\rm AC}\sin(\omega_{\rm AC}t)]dt = \Gamma_0 I_0(\beta e S_{\rm AC}), \tag{B4}$$

where

$$I_0(x) = \sum_{s=0}^{\infty}\frac{1}{s!s!}\left(\frac{x}{2}\right)^{2s}. \tag{B5}$$

When $\beta S_{\rm AC} \ll 1$, Eq. (B4) is simplified to

$$\frac{\overline{\Gamma^+}}{\Gamma_0} \sim 1 + \frac{1}{4}(\beta e S_{\rm AC})^2. \tag{B6}$$

Using Eqs. (B3) and (B6), and the Taylor expansion, Eqs. (B2) and (B1) can be converted to

$$\tau_{\rm th} \sim \frac{\langle N_{\rm SS}\rangle}{\overline{\Gamma^+}}\frac{4}{(\beta e S_{\rm AC})^2}\ln\left(\frac{1}{1-a}\right), \tag{B7}$$

$$\langle N(t)\rangle \sim \frac{\langle N_{\rm SS}\rangle(\beta e S_{\rm AC})^2}{4\ln(\overline{\Gamma^+}/\Gamma_0)}[1-\exp(-2\beta E_{\rm C}\overline{\Gamma^+}t)], \tag{B8}$$

respectively. Equation (B8) represents the transient characteristics with a time constant of $(2\beta E_{\rm C}\overline{\Gamma^+})^{-1}$.

When $\beta S_{\rm AC} \gg 1$, the asymptotic form of the Bessel functions simplifies Eq. (B4) to

$$\frac{\overline{\Gamma^+}}{\Gamma_0} = \frac{\exp(\beta e S_{\rm AC})}{\sqrt{2\pi\beta e S_{\rm AC}}}\left\{1 + \frac{1}{8\beta e S_{\rm AC}} + \mathcal{O}\left[\frac{1}{(\beta S_{\rm AC})^2}\right]\right\} \sim \frac{\exp(\beta e S_{\rm AC})}{\sqrt{2\pi\beta e S_{\rm AC}}}. \tag{B9}$$

Using Eqs. (B2), (B3), and (B9) and $\ln(\overline{\Gamma^+}/\Gamma_0) \sim \beta e S_{\rm AC}$,

$$\tau_{\rm th} \sim \frac{\langle N_{\rm SS}\rangle}{\overline{\Gamma^+}}a. \tag{B10}$$

APPENDIX C: HOUSEKEEPING HEAT IN AN NESS

Since $\langle \dot{Q}^{\rm SS}_{\rm HK}\rangle$ is equal to $\langle \dot{Q}^{\rm SS}_{\rm T}\rangle$, shown in Eq. (12), in an NESS, its time-average can be given by

$$\langle \dot{Q}^{\rm SS}_{\rm HK}\rangle = -\frac{\omega_{\rm AC}}{2\pi}\int_0^{2\pi/\omega_{\rm AC}} e S_{\rm AC}\sin(\omega_{\rm AC}t) \times \Gamma_0\exp[-e S_{\rm AC}\sin(\omega_{\rm AC}t)]dt = \Gamma_0 e S_{\rm AC} I_1(\beta e S_{\rm AC}), \tag{C1}$$

where

$$I_1(x) = \sum_{s=0}^{\infty}\frac{1}{s!(s+1)!}\left(\frac{x}{2}\right)^{(2s+1)} \tag{C2}$$

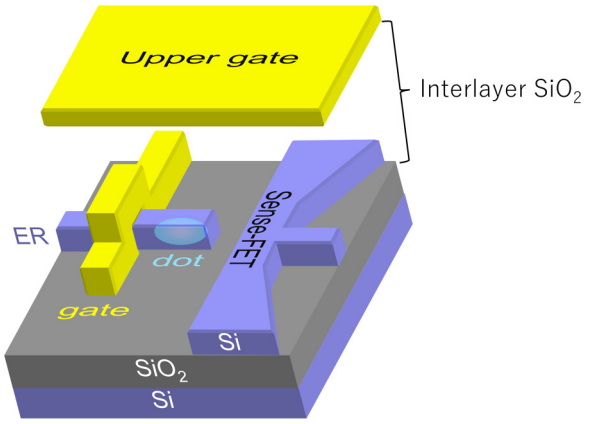


FIG. 7. Schematic view of the device structure.

is the integral formula for the modified Bessel function. When $\beta e S_{\rm AC} \ll 1$, Eq. (B6) and the Taylor series expansion approximate Eq. (C1):

$$\langle \dot{Q}^{\rm SS}_{\rm HK}\rangle \sim \Gamma_0 e S_{\rm AC}\left[\frac{1}{2}(\beta e S_{\rm AC}) + \frac{1}{16}(\beta e S_{\rm AC})^3\right] = \Gamma_0\frac{(\beta e S_{\rm AC})^2}{2\beta}\left[1 + \frac{1}{8}(\beta e S_{\rm AC})^2\right] \sim 4E_{\rm C}\langle N_{\rm SS}\rangle\overline{\Gamma^+}. \tag{C3}$$

When $\beta e S_{\rm AC} \gg 1$, the asymptotic form of the modified Bessel functions, Eq. (B9), and $\ln(\overline{\Gamma^+}/\Gamma_0) \sim \beta e S_{\rm AC}$ simplify Eq. (C1) to

$$\langle \dot{Q}^{\rm SS}_{\rm HK}\rangle \sim \Gamma_0 e S_{\rm AC}\frac{\exp(\beta e S_{\rm AC})}{\sqrt{2\pi\beta e S_{\rm AC}}} \sim 2E_{\rm C}\langle N_{\rm SS}\rangle\overline{\Gamma^+}. \tag{C4}$$

APPENDIX D: DEVICE STRUCTURE

The device structure is fabricated from a silicon-on-insulator (SOI) wafer with a buried oxide thickness of 400 nm [see Fig. 7]. The width and height of the SOI wire connected to a dot and ER were about 10 nm. The gate length of a gate made of polycrystalline silicon was about 10 nm. The width and height of the constriction part of the SOI channel of the sense-FET were around 10 nm. An upper gate covering the whole area shown by the scanning-electron-microscope image controls the current flowing through the sense-FET, and it induces electrons in the ER.

Since all measurements are carried out at room temperature, the energy level spacing in the dot due to quantum confinement is negligible compared to thermal energy.

[1] R. Landauer, Irreversibility and heat generation in the computing process, IBM J. Res. Dev. **5**, 183 (1961).

[2] A. Bérut, A. Arakelyan, A. Petrosyan, S. Ciliberto, R. Dillenschneider, and E. Lutz, Experimental verification of Landauer's principle linking information and thermodynamics, Nature (London) **483**, 187 (2012).

[3] Y. Jun, M. Gavrilov, and J. Bechhoefer, High-precision test of Landauer's principle in a feedback trap, Phys. Rev. Lett. **113**, 190601 (2014).

[4] J. V. Koski, V. F. Maisi, J. P. Pekola, and D. V. Averin, Experimental realization of a Szilard engine with a single electron, Proc. Natl. Acad. Sci. USA **111**, 13786 (2014).

[5] A. Bérut, A. Petrosyan, and S. Ciliberto, Information and thermodynamics: Experimental verification of Landauer's erasure principle, J. Stat. Mech. (2015) P06015.

[6] L. Martini, M. Pancaldi, M. Madami, P. Vavassori, G. Gubbiotti, S. Tacchi, F. Hartmann, M. Emmerling, S. Höfling, L. Worschech, and G. Carlotti, Experimental and theoretical analysis of Landauer erasure in nano-magnetic switches of different sizes, Nano Energy **19**, 108 (2016).

[7] J. Hong, B. Lambson, S. Dhuey, and J. Bokor, Experimental test of Landauer's principle in single-bit operations on nanomagnetic memory bits, Sci. Adv. **2**, e1501492 (2016).

[8] D. Barker, M. Scandi, S. Lehmann, C. Thelander, K. A. Dick, M. Perarnau-Llobet, and V. F. Maisi, Experimental verification of the work fluctuation-dissipation relation, Phys. Rev. Lett. **128**, 040602 (2022).

[9] N. Shiraishi, K. Saito, and H. Tasaki, Universal trade-off relation between power and efficiency for heat engines, Phys. Rev. Lett. **117**, 190601 (2016).

[10] D. H. Wolpert, The stochastic thermodynamics of computation, J. Phys. A: Math. Theor. **52**, 193001 (2019).

[11] K. Proesmans, J. Ehrich, and J. Bechhoefer, Finite-time Landauer principle, Phys. Rev. Lett. **125**, 100602 (2020).

[12] J. S. Lee, S. Y. Lee, H. Kwon, and H. Park, Speed limit for a highly irreversible process and tight finite-time Landauer's bound, Phys. Rev. Lett. **129**, 120603 (2022).

[13] M. Esposito and C. Van den Broeck, Second law and Landauer principle far from equilibrium, Europhys. Lett. **95**, 40004 (2011).

[14] Y. Oono and M. Paniconi, Steady state thermodynamics, Prog. Theor. Phys. Suppl. **130**, 29 (1998).

[15] T. Hatano and S.-i. Sasa, Steady-state thermodynamics of Langevin systems, Phys. Rev. Lett. **86**, 3463 (2001).

[16] M. Esposito, U. Harbola, and S. Mukamel, Entropy fluctuation theorems in driven open systems: Application to electron counting statistics, Phys. Rev. E **76**, 031132 (2007).

[17] K. Yoshimura, A. Kolchinsky, A. Dechant, and S. Ito, Housekeeping and excess entropy production for general nonlinear dynamics, Phys. Rev. Res. **5**, 013017 (2023).

[18] U. Seifert, Entropy production along a stochastic trajectory and an integral fluctuation theorem, Phys. Rev. Lett. **95**, 040602 (2005).

[19] P. Gaspard, Fluctuation theorem for nonequilibrium reactions, J. Chem. Phys. **120**, 8898 (2004).

[20] T. Speck and U. Seifert, Integral fluctuation theorem for the housekeeping heat, J. Phys. A: Math. Gen. **38**, L581 (2005).

[21] C. Van den Broeck and M. Esposito, Three faces of the second law. II. Fokker-Planck formulation, Phys. Rev. E **82**, 011144 (2010).

[22] M. Esposito and C. Van den Broeck, Three faces of the second law. I. Master equation formulation, Phys. Rev. E **82**, 011143 (2010).

[23] D. V. Averin and J. P. Pekola, Statistics of the dissipated energy in driven single-electron transitions, Europhys. Lett. **96**, 67004 (2011).

[24] B. Küng, C. Rössler, M. Beck, M. Marthaler, D. S. Golubev, Y. Utsumi, T. Ihn, and K. Ensslin, Irreversibility on the level of single-electron tunneling, Phys. Rev. X **2**, 011001 (2012).

[25] O. P. Saira, Y. Yoon, T. Tanttu, M. Möttönen, D. V. Averin, and J. P. Pekola, Test of the Jarzynski and Crooks fluctuation relations in an electronic system, Phys. Rev. Lett. **109**, 180601 (2012).

[26] J. P. Pekola and O. P. Saira, Work, free energy and dissipation in voltage driven single-electron transitions, J. Low. Temp. Phys. **169**, 70 (2012).

[27] A. Hofmann, V. F. Maisi, C. Rössler, J. Basset, T. Krähenmann, P. Märki, T. Ihn, K. Ensslin, C. Reichl, and W. Wegscheider, Equilibrium free energy measurement of a confined electron driven out of equilibrium, Phys. Rev. B **93**, 035425 (2016).

[28] A. Hofmann, V. F. Maisi, J. Basset, C. Reichl, W. Wegscheider, T. Ihn, K. Ensslin, and C. Jarzynski, Heat dissipation and fluctuations in a driven quantum dot, Phys. Status Solidi B **254**, 1600546 (2017).

[29] E. H. Trepagnier, C. Jarzynski, F. Ritort, G. E. Crooks, C. J. Bustamante, and J. Liphardt, Experimental test of Hatano and Sasa's nonequilibrium steady-state equality, Proc. Natl. Acad. Sci. USA **101**, 15038 (2004).

[30] A. Mounier and A. Naert, The Hatano-Sasa equality: Transitions between steady states in a granular gas, Europhys. Lett. **100**, 30002 (2012).

[31] T. Ando and T. Otsu-Hyodo, Nonequilibrium heat dissipation as a probe for detecting wavefront distortion in microscopy, Phys. Rev. Res. **6**, 043263 (2024).

[32] K. Nishiguchi, Y. Ono, and A. Fujiwara, Single-electron thermal noise, Nanotechnology **25**, 275201 (2014).

[33] P.-A. Carles, K. Nishiguchi, and A. Fujiwara, Deviation from the law of energy equipartition in a small dynamic-random-access memory, Jpn. J. Appl. Phys. **54**, 06FG03 (2015).

[34] K. Nishiguchi, C. Koechlin, Y. Ono, A. Fujiwara, H. Inokawa, and H. Yamaguchi, Single-electron-resolution electrometer based on field-effect transistor, Jpn. J. Appl. Phys. **47**, 8305 (2008).

[35] K. Nishiguchi, Y. Ono, and A. Fujiwara, Single-electron counting statistics of shot noise in nanowire Si metal-oxide-semiconductor field-effect transistors, Appl. Phys. Lett. **98**, 193502 (2011).

[36] C. Salhani, K. Chida, T. Shimizu, T. Hayashi, and K. Nishiguchi, Alternating-current signal sensing beyond cutoff frequency using a single-electron dynamic random access memory, Phys. Rev. Appl. **23**, L021001 (2025).

[37] H. A. Kramers, Brownian motion in a field of force and the diffusion model of chemical reactions, Physica **7**, 284 (1940).

[38] O. Raz, Y. Subaşı, and C. Jarzynski, Mimicking nonequilibrium steady states with time-periodic driving, Phys. Rev. X **6**, 021022 (2016).

[39] A. Datta, P. Pietzonka, and A. C. Barato, Second law for active heat engines, Phys. Rev. X **12**, 031034 (2022).